Chapter 5
Hyperbolic Metamaterials for Single-Photon Sources and Nanolasers

M.Y. Shalaginov, R. Chandrasekar, S. Bogdanov, Z. Wang, X. Meng, O.A. Makarova, A. Lagutchev, A.V. Kildishev, A. Boltasseva and V.M. Shalaev

Abstract Hyperbolic metamaterials are anisotropic media that behave as metals or as dielectrics depending on light polarization. These plasmonic materials constitute a versatile platform for promoting both spontaneous and stimulated emission for a broad range of emitter wavelengths. We analyze experimental realizations of a single–photon source and of a plasmonic laser based on two different architectures of hyperbolic metamaterials. At the heart of this material capability lies the high broadband photonic density of states originating from a rich structure of confined plasmonic modes.

M.Y. Shalaginov (✉) · R. Chandrasekar · S. Bogdanov · Z. Wang · X. Meng · O.A. Makarova · A. Lagutchev · A.V. Kildishev · A. Boltasseva · V.M. Shalaev
School of Electrical & Computer Engineering, Birck Nanotechnology Center, and Purdue Quantum Center, Purdue University, West Lafayette, IN 47907, USA
e-mail: shalaginov@purdue.edu

R. Chandrasekar
e-mail: chandrar@purdue.edu

S. Bogdanov
e-mail: sbogdan@purdue.edu

Z. Wang
e-mail: wang1973@purdue.edu

X. Meng
e-mail: meng14@purdue.edu

O.A. Makarova
e-mail: omakarov@purdue.edu

A. Lagutchev
e-mail: lagutch@purdue.edu

A.V. Kildishev
e-mail: kildishev@purdue.edu

A. Boltasseva
e-mail: aeb@purdue.edu

V.M. Shalaev
e-mail: shalaev@purdue.edu

S.I. Bozhevolnyi et al. (eds.), *Quantum Plasmonics*,
Springer Series in Solid-State Sciences 185,
DOI 10.1007/978-3-319-45820-5_5

5.1 Introduction

The advent of nanofabrication has opened entirely new ways for designing optical materials, by virtue of the freedom to generate meta-atoms smaller than the wavelength with tailored electromagnetic responses. This has allowed for improved spatial control of bulk parameters, such as permittivity and permeability, and to engineer the dispersion of optical materials with properties unavailable in nature, termed as optical metamaterials. Metamaterials offer new avenues for manipulation of light, leading to such unusual applications as high-resolution imaging, high-resolution lithography, and emission lifetime engineering. This chapter is focused on a subclass of metamaterials exhibiting hyperbolic dispersion that serves as a flexible platform for engineering optical phenomena.

Hyperbolic metamaterials (HMM), uniaxial nanostructured materials that combine the properties of transparent dielectrics and reflective metals, first attracted the attention of researchers in the middle of last century. These efforts were stimulated by the problem of propagation of radio waves in the Earth's ionosphere [1, 2], and, more generally, by the behavior of the electromagnetic waves in a plasma of electrons and ions upon the applied permanent magnetic field. Along with the anisotropic plasmas, stratified man-made hyperbolic materials were studied for radiofrequency applications of transmission lines [3].

Hyperbolic composites (also known as media with indefinite permittivity and permeability tensors [4]) and some homogeneous materials with hyperbolic dispersion were experimentally realized across the optical spectrum, from UV to visible, and from near-IR to mid-IR frequencies. Subwavelength imaging [5, 6], high-resolution lithography [7], lifetime engineering [8], and new approaches to

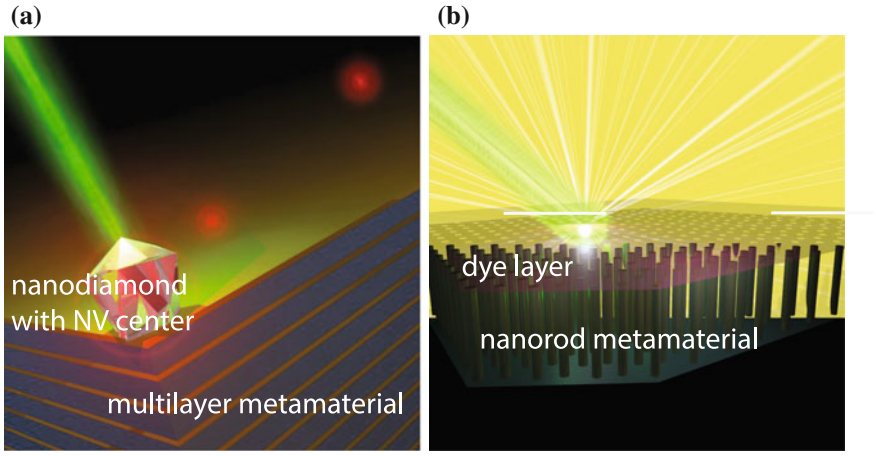

Fig. 5.1 Illustration of **a** multilayer hyperbolic superlattices for enhancing emission properties of single color centers in *diamond* and **b** hyperbolic nanorod arrays for lasing action with dye molecules. Figures reproduced with permission: **a** courtesy of N. Kinsey, **b** [13] from Copyright 2016 ACS

enhance the nonlinear response [9] of optical structures, have all been demonstrated in hyperbolic structures. Hyperbolic media continue to be of great interest to the research community with possible applications emerging in heat transport [10] and acoustics [11]. Although hyperbolic materials also exist naturally, their applications in the visible range are limited by losses and fixed bandwidth [12].

In this chapter, we first discuss the physics of light-matter interaction in hyperbolic metamaterials. Secondly, we consider how multilayer-based metamaterials could enhance the emission from single atom-like defects, such as color centers in diamond (see Fig. 5.1a). Next, we provide experimental observation of lasing using nanorod-based HMMs (see Fig. 5.1b) and corresponding theoretical interpretations.

5.2 Fundamentals of Hyperbolic Metamaterials

Oscillating electric dipoles placed inside or in the vicinity of HMMs see their radiated power enhanced over a broad spectral range. This enhancement is a result of a broadband singularity in the photonic local density of states (LDOS) within the HMM [8]. The photonic LDOS, similar to its electronic counterpart, can be quantified as the volume in k-space between iso-frequency surfaces. For extraordinary waves in a uniaxial anisotropic medium with dielectric tensor $\vec{\vec{\varepsilon}} = diag[\varepsilon_{\parallel}, \varepsilon_{\parallel}, \varepsilon_{\perp}]$, the iso-frequency surfaces are defined by the following equation:

$$\omega^2/c^2 = k_{\parallel}^2/\varepsilon_{\perp} + k_{\perp}^2/\varepsilon_{\parallel}$$

where subscripts $\perp$ and $\parallel$ indicate the directions perpendicular and parallel to the surface plane, respectively. In the case of dielectric materials with $\varepsilon_{\perp}, \varepsilon_{\parallel} > 0$, LDOS is equivalent to the volume of an infinitesimally thin spheroidal shell in k-space (see Fig. 5.1a) that separates two neighboring iso-frequency surfaces. However, in a medium with extreme optical anisotropy, $\varepsilon_{\perp}$ and $\varepsilon_{\parallel}$ are of opposite signs which produces a hyperboloidal shell, two-sheeted (type I, see Fig. 5.2b) or one-sheeted (type II, see Fig. 5.2c), whose volume is infinitely large (i.e. broadband singularity in LDOS appears). As a result, such a medium allows the propagation of high-k modes with arbitrarily large wavevectors. This hyperbolic regime can be engineered to exist over a broad wavelength range.

The HMM can be practically realized as either a lamellar structure consisting of alternating subwavelength-thick layers of metallic and dielectric materials [14] (see Fig. 5.1a) or as an array of metal nanorods embedded into a dielectric host matrix [15] (see Fig. 5.1b). Both HMM implementations can be well described in the approximation of effective medium theory (EMT). Corresponding expressions for effective permittivities are provided in the Table 5.1. In some cases, the fields in the metamaterials can exhibit strong spatial variation resulting in a nonlocal response. Hence special corrections should be introduced into the EMT formulas [16, 17].

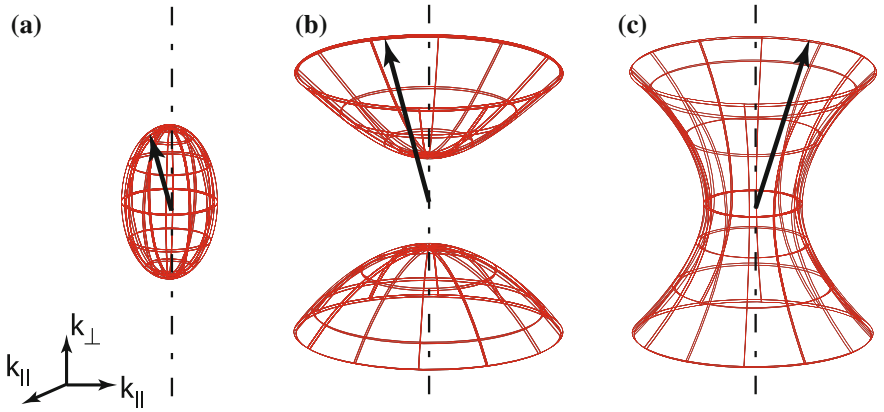

Fig. 5.2 Iso-frequency surfaces in *k*-space for uniaxial media: **a** spheroid in the case of an anisotropic dielectric ($\varepsilon_\perp, \varepsilon_\parallel > 0$), **b**, **c** hyperboloids (type I and II, respectively) in the cases of extremely anisotropic media ($\varepsilon_\perp < 0$, $\varepsilon_\parallel > 0$ (**b**); $\varepsilon_\perp > 0$, $\varepsilon_\parallel < 0$ (**c**))

Table 5.1 Components of permittivity tensor as defined by effective medium theory (EMT) for metal-dielectric metamaterials implemented as metal nanorod arrays in a dielectric matrix and as a stack of alternating layers of metal and dielectric

Nanorod array		Multilayer stack	
$\varepsilon_\perp = \varepsilon_m f + \varepsilon_d(1-f)$	(1)	$\varepsilon_\perp = \frac{\varepsilon_m \varepsilon_d}{\varepsilon_d f + \varepsilon_m(1-f)}$	(3)
$\varepsilon_\parallel = \varepsilon_d \frac{\varepsilon_m(1+f)+\varepsilon_d(1-f)}{\varepsilon_m(1-f)+\varepsilon_d(1+f)}$	(2)	$\varepsilon_\parallel = \varepsilon_m f + \varepsilon_d(1-f)$	(4)

This broadband optical anisotropy and the resulting high photonic density of states in HMMs can be utilized for engineering integrated optical devices such as deterministic single-photon sources [18] and plasmonic lasers [19].

5.3 Enhancement of Single-Photon Emission from Color Centers in Diamond

The photon is a workhorse of quantum information processing [20], including quantum computation [21], quantum cryptography [22], quantum communication [23] and teleportation [24]. Generation and detection of single photons using quantum emitters plays an important role in applied aspects of quantum photonics.

Over the past 10 years, numerous types of deterministic single-photon sources have been demonstrated [18], including trapped atoms and ions, single molecules, color centers, atomic ensembles, quantum dots, and mesoscopic quantum wells. A nitrogen-vacancy (NV) color center in diamond, formed by a substitutional

nitrogen atom and a vacancy at an adjacent lattice site, is of particular interest for photonic quantum technologies [25]. As a single-photon source, it is resistant against photobleaching and operates in the single-photon regime at room temperature [26]. Additionally, an NV center can be well localized, its intrinsic quantum yield is close to unity [25], and its optical transition can be tuned via external electric [27] and/or magnetic fields [28].

The applications of an NV center as a single-photon generator and spin-photon interface could substantially benefit from an enhanced emission rate and collection efficiency. An emission rate enhancement can be achieved by engineering the electromagnetic environment of the emitter utilizing the Purcell effect [29]. So far, this has been accomplished by using resonant photonic structures, such as microspherical resonators [30], photonic crystal microcavities [31], and photonic crystal nanobeams [32], which are all bandwidth limited. Coupling NV centers to HMMs [33, 34] allows for taking advantage of the entire defect radiation spectrum. The HMM provides numerous extra decay channels in a broad spectral range for the coupled emitter [33, 35, 36, 37]. The excitation is transferred into high–k metamaterial modes which result from hybridization of surface plasmon polaritons at the interfaces of the layers constituting the HMM. The high-k waves could be further outcoupled into free space and significantly contribute to the emission signal [35, 37].

For enhancing the NV center emission we epitaxially grew a hyperbolic metamaterial superlattice composed of plasmonic titanium nitride (TiN) and dielectric aluminum scandium nitride ($Al_xSc_{1-x}N$) [14]. TiN is a novel plasmonic material known for its CMOS compatibility, mechanical strength, and thermal stability at high temperatures (melting point >2700°C) [38]. This material can be epitaxially deposited on a variety of different substrates, such as magnesium oxide, aluminum scandium nitride, and c-sapphire, in the form of ultra–thin (<5 nm) films. Successful material deposition with such small thicknesses is of fundamental importance for achieving a significant increase in LDOS, since the LDOS for a multilayer HMM is inversely related to the cube of the layer thickness [39].

Nanodiamonds used in this experiments were dispersed on the HMM surface and had an average size of 50 nm as shown by the SEM scan in Fig. 5.3. NV center emission was collected using high numerical aperture oil immersion objective. A 60-nm–thick layer of polyvinyl alcohol (PVA, 1.5 % w/v) was deposited on top of the sample to immobilize and separate nanodiamonds from the immersion oil. The immersion oil was needed for efficient collection of emitted light by an objective lens with the high numerical aperture.

Nanodiamonds were also deposited by the same method onto standard 150 μm–thick glass coverslips, which were used as control samples. Since the refractive indices of these glass substrates (1.53), immersion oil (1.52) and PVA layer (1.50) were closely matching, the nanodiamonds in the reference samples were effectively immersed into an infinite homogeneous medium with a refractive index of ∼1.5.

A $TiN/Al_{0.7}Sc_{0.3}N$ superlattice was epitaxially grown on a 0.5-mm-thick, [001]–oriented magnesium oxide (MgO) substrate using reactive DC magnetron sputtering at 750 °C. The metamaterial was implemented as an epitaxial stack of 10 pairs of layers each consisting of an 8.5-nm-thick film of TiN and a 6.3-nm-thick film of

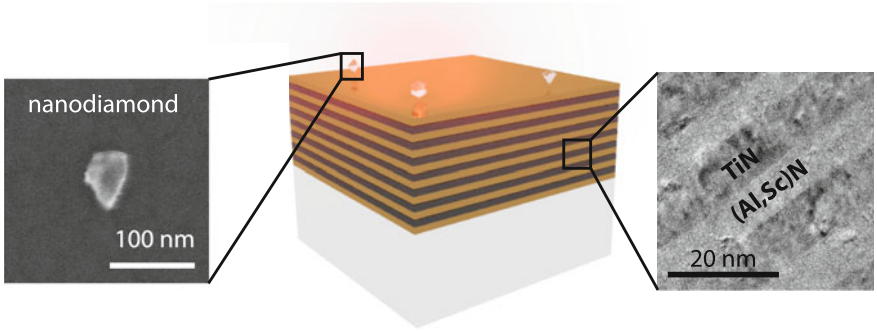

Fig. 5.3 *Center* sample structure composed of TiN/(Al,Sc)N superlattice grown on *top* of MgO and nanodiamonds spin-coated on *top* of the superlattice. *Left* SEM scan of nanodiamonds on *top* of the HMM sample. Average nanodiamond size was 50 nm. *Right* cross-sectional TEM image of TiN-$Al_{0.7}Sc_{0.3}N$ superlattice. Thicknesses of TiN and $Al_{0.7}Sc_{0.3}N$ layers are 8.5 nm and 6.3 nm, respectively

$Al_{0.7}Sc_{0.3}N$. Figure 5.3 demonstrates the cross-sectional TEM image of the superlattice. Since the superlattice layer thicknesses are much smaller than the wavelength of operation (600–800 nm), the HMM can be approximated as a uniaxial anisotropic effective medium with dielectric functions $\varepsilon_{\parallel}$ and $\varepsilon_{\perp}$. The optical constants of the HMM were measured using spectroscopic ellipsometry. The TiN/(Al,Sc)N metamaterial exhibited hyperbolic dispersion with $\varepsilon_{\perp} = 16.4 + i21.1$, $\varepsilon_{\parallel} = -2.3 + i2.1$ at 685 nm, which is the peak emission wavelength of the NV center. Thus, for the electric field, parallel to the interface, the metamaterial at this wavelength behaved as a metal. As an additional benefit, at the excitation

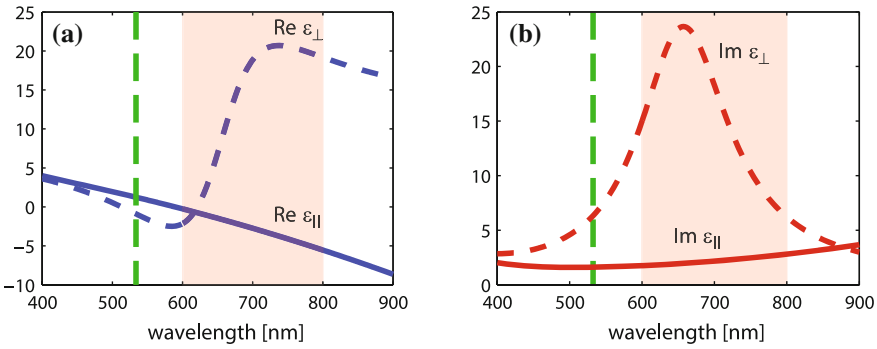

Fig. 5.4 **a** Real and **b** imaginary parts of the dielectric functions of the uniaxial effective medium that approximates the fabricated HMM. The permittivities were obtained by spectroscopic ellipsometry in the spectral range 400–900 nm. Within the range of the NV center emission (600–800 nm-highlighted), the metamaterial shows hyperbolic dispersion ($\mathrm{Re}[\varepsilon_{\perp}] > 0$, $\mathrm{Re}[\varepsilon_{\parallel}] < 0$). At the excitation wavelength (532 nm, *green line*) the metamaterial behaves as a lossy dielectric. Figures reproduced with permission: [33] from Copyright 2015 Wiley-VCH

wavelength of 532 nm (Fig. 5.4, vertical dashed green line) the TiN/(Al,Sc)N metamaterial behaved as a lossy dielectric allowing the penetration of the tangential component of electric field through the HMM to the emitter.

5.3.1 Calculations of NV Emission Enhancement by HMM

In general, to estimate both the enhancement of the spontaneous emission rate (represented by Purcell factor F_P) and normalized collected emission power f_{rad} one may utilize a semiclassical treatment, where the emitter levels are quantized. Since in our experimental lifetime measurement the quantum emitter is weakly coupled to the metamaterial environment, the results are expected to be in a good agreement with the treatment based on classical electrodynamics [40]. We therefore consider the problem of classical dipole radiation near a planar layered medium, which is described in more detail in [41].

The inset in Fig. 5.5a shows the modelled configuration, which consists of an oscillating dipole elevated at height h above the HMM uppermost layer ($Al_{0.7}Sc_{0.3}N$), the upper half-space (superstrate) with refractive index 1.515 ($\varepsilon_{sup} = 2.295$ simulating PVA/immersion oil), planar multilayer TiN/(Al,Sc)N superlattice ($\varepsilon_m/\varepsilon_d$) and the lower half-space (substrate) made of MgO (ε_{sub}). For this simulation we considered the fabricated HMM composed of 10 pairs of 8.5-nm-thick TiN and 6.3-nm-thick $Al_{0.7}Sc_{0.3}N$ on MgO substrate. The layer thicknesses were chosen to provide optimal performance, which was previously discussed in [14]. The formulas used to calculate the Purcell factor F_P and

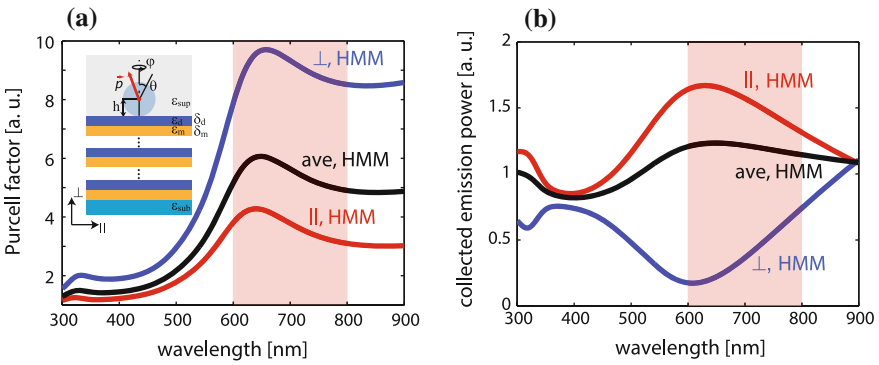

Fig. 5.5 Theoretical estimations of Purcell factor (**a**) and collected emission power (**b**) for a dipole located in immersion oil/PVA ($\varepsilon_{sup} = 2.295$) 25 nm above the HMM surface. *Blue*, *red* and *black curves* correspond to the dipole orientations perpendicular (⊥), parallel (||) to the HMM interface and averaged (ave), respectively. *Highlighted area* indicates the emission spectral range of NV center at room temperature. Collection angle is 79.6°, which corresponds to NA 1.49. Layout of the calculated structure is shown in the inset. Figures reproduced with permission: [33] from Copyright 2015 Wiley-VCH

normalized collected emission power f_{rad} for the dipole orientations: in-plane (∥), perpendicular (⊥), and averaged (ave), statistical average over all possible orientations, are given in the Appendix.

The collection angle ($\theta_{max} = 79.6°$) is defined by the numerical aperture of the objective lens (NA = 1.49). The generalized Fresnel's reflection coefficients $\tilde{r}^p$ and $\tilde{r}^s$ for the superlattice were calculated utilizing the recursive imbedding method [42], which is more precise and efficient than the direct transfer matrix approach. Normalization factors included into F_P and f_{rad} are the total radiation power and the power emitted into the collection angle, respectively. Both quantities corresponded to the case of the emitter immersed into a homogeneous medium with dielectric permittivity ε_{sup}, which is a reasonable approximation for the normalization procedure employed in the experiment.

The results of the calculations are demonstrated in Fig. 5.5. Assuming that the NV center is located at the crystal center, the expected Purcell factor (or change in lifetime) for the nanodiamonds with a mean diameter of 50 nm should be on average around 4.5 (we note that placing NV centers closer to the HMM surface can significantly increase the Purcell factor making it on the order of 10^2—see Fig. 5.10). The detected count rates corresponding to the normalized collected emission power for the same type of nanodiamonds are anticipated to increase on average by about 20 percent.

5.3.2 *Experimental Demonstration of HMM Enhanced Single-Photon Emission*

We have optically examined the samples described earlier consisting of collection of nanodiamond-based NV centers dispersed on HMM surface. A control sample was used, in which the nanodiamonds were dispersed on a coverslip glass substrate, whose refractive index matched that of the objective oil. Since we aim at fabricating and testing a single–photon source, we must ensure that the emitters are single, i.e. cannot emit more than one photon at a time. In order to select nanodiamonds with single NV centers, we first measured the second–order correlation function $g^{(2)}(t)$ of the detected fluorescence spots. Only NV centers with $g^{(2)}(0)$ significantly less than 0.5 were considered for further experiments. The typical measured second-order correlation functions showing photon antibunching effect are shown for a single NV center on the glass coverslip and on the HMM in Fig. 5.6.

We retrieved the total decay lifetimes of the NV centers from the exponential fitting of the fluorescence decays such as the ones shown in Fig. 5.7a. The average values measured were 17.1 and 4.3 ns on glass and HMM, respectively (see Fig. 5.7b). Hence, the NVs on HMM exhibit an average decrease in lifetime by a factor of 4 compared to NVs on coverslip, which is consistent with the above calculations. The lowest recorded lifetime for a single NV center on top of the HMM was 1.5 ns, which corresponds to a Purcell factor of 11.4. The spreads in the

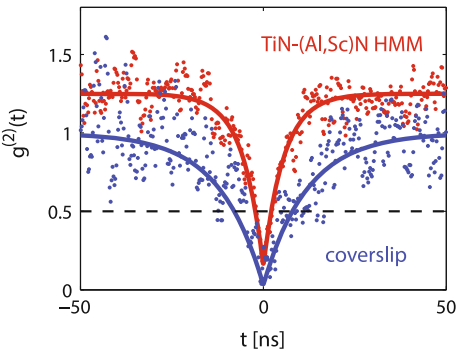

Fig. 5.6 Second-order correlation function $g^{(2)}(t)$ of a representative nanodiamond with single NV center on *top* of HMM. Figure reproduced with permission: [33] from Copyright 2015 Wiley-VCH

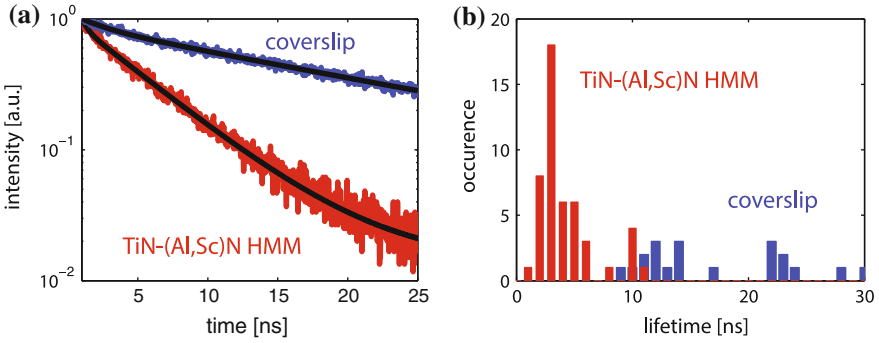

Fig. 5.7 **a** Representative normalized fluorescence decays and **b** histograms of lifetimes for the NV centers located on glass coverslip (reference sample) and on HMM. The average and largest decreases in lifetime are 4 and 11.4, respectively. Figures reproduced with permission: [33] from Copyright 2015 Wiley-VCH

lifetime statistics are likely due to the variation in nanodiamond size, NV center dipole orientation and its distance from the HMM surface.

Finally, we measured the dependence of the single-photon emission rate from the NV centers versus the excitation power. In Fig. 5.8a, we show these dependences for the brightest NV centers on both the HMM and the glass coverslip. Both dependences have been corrected for the background emission. The total count rate was measured at the NV center site and the background count rate was measured at a nanodiamond-free location. Saturation of the emission count rate was observed around 1 mW of the pump power. The experimentally measured saturation curves were fitted using the expression $I(P) = I_0/(1 + P_{sat}/P)$ [43] and yielded the saturated single–photon count rates for each individual NV center. The histogram of the saturated single–photon count rates are shown in Fig. 5.8b for NV centers both on

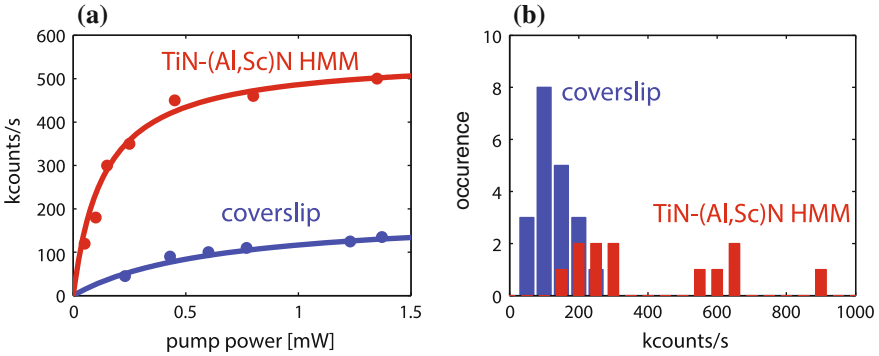

Fig. 5.8 Collected single-photon count rates (corrected for background emission) from NV centers in 50 nm nanodiamonds. **a** Typical saturation curves and **b** histograms of count rates for nanodiamonds on glass coverslip (*blue*) and HMM (*red*). The average enhancements for the first and second statistical maxima are 1.8 and 4.7, respectively. Figures reproduced with permission: [33] from Copyright 2015 Wiley-VCH

glass and the HMM. The histogram displays multiple maxima. For the one around 200 kcounts/s, the average enhancement against the coverslip was 1.8 ± 1.1. This is consistent with predicted value of 1.2, within the error margin. The variation of the enhancement is large because count rates for both HMM and coverslip substrates have significant spreads. The next maximum in the histogram corresponds to an average count rate enhancement of 4.7 ± 2.2. This number is beyond the theory prediction for a planar HMM. Finally, one diamond shows even higher count rate enhancement. The obtained statistics suggests the existence of an additional mechanism responsible for extra enhancement.

5.3.3 *Increasing Collection Efficiency by Outcoupling High-k Waves to Free Space*

We have seen in the simulations of planar HMM presented above that a high Purcell factor did not translate into a higher collected emission power (see Fig. 5.5) because the optical power residing in the high-k metamaterial modes was not outcoupled to free space. However, our experiments (see Fig. 5.8b) indicate that one can in practice collect much more power than what is predicted by theory (see Fig. 5.5).

To get at least a qualitative understanding of this phenomenon we have employed an additional computational effort. For this, we assumed that excessive emission rates from certain nanodiamonds potentially could arise from the influence of either neighboring superlattice defects or adjacent “dark” nanodiamonds lacking NV centers. The proposed mechanism is as follows: HMMs can support surface plasmon-polaritons (SPPs) and bulk electromagnetic modes, both having high propagation constant (high-k modes) [44]. It is known that an excited emitter located in the vicinity of HMM surface has a high probability of transferring energy into such high-k modes [39]. Once excited, these high-k waves propagate through

the HMM, never leaving the bulk medium where they are eventually absorbed and do not provide any contribution to the collected photon flux. However, the presence of the surface defects or scattering objects may result in outcoupling of these modes into the far field and therefore provide additional contribution to the emitted signal.

To verify this assumption both substrate defects and "dark" nanodiamonds were modelled as 50-nm-diameter spheres with varied separation from emitting dipole. In essence, the calculation indeed demonstrated that the presence of the dark nanodiamond and TiN particle results in further enhancements of emission rate by factors of 1.3 and 2.0, respectively compared to a perfect HMM surface. This result does support the experimental observations though it clearly requires further rigorous investigation. In particular, instead of relying on random irregularities of the HMM surface, one can place emitting nanodiamonds next to engineered nanostructures with optimized outcoupling efficiency. Our calculations show that the portion of NV center emission coupled into the metamaterial could be quite efficiently recovered prior to dissipation in the HMM. This emission could be directed into the far-field by using even very basic structures, such as gratings, nanodisks, nanoholes, etc.

An example of such artificially created structure is a single circular groove milled in the HMM around the nanodiamond (see Fig. 5.9a). The groove can outcouple the propagating metamaterial modes at its sharp corners. The structure with optimized geometry promises a several times increase in collected power in comparison with a NV center on a coverslip. A simulation using finite-element method (see Fig. 5.9b) showed that for in-plane oriented dipole, the structure should consist of a 100 nm radius cylinder surrounded by a 250 nm wide groove. An additional factor that helps to increase the collected power is the use of a TiN reflecting layer between the MgO substrate and the HMM. The simulation for

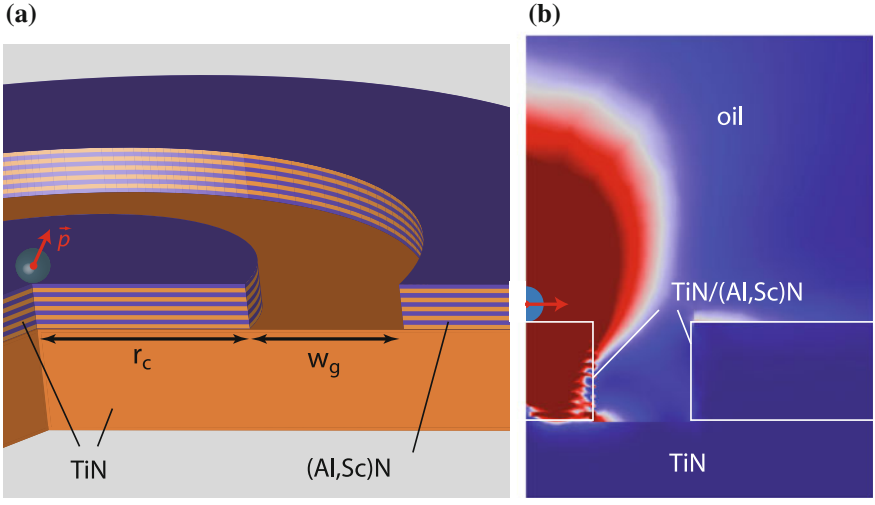

Fig. 5.9 **a** Schematic of a circular groove milled in HMM around a nanodiamond to improve the collected power in the far-field (in 60° aperture angle) by scattering the high-k modes propagating along the surface and inside HMM. **b** Distribution of power density amplitude for the in-plane oriented NV center

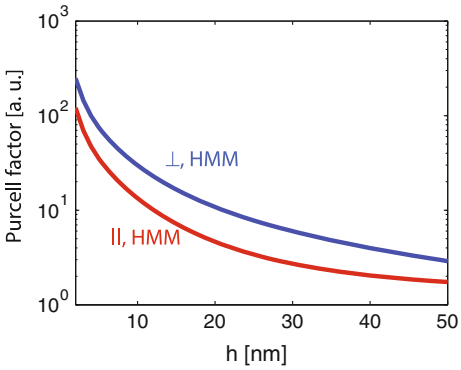

Fig. 5.10 Dependence of the Purcell factor F_P on a dipole position h above the HMM surface. Values of F_P are obtained by averaging the characteristics (shown in Fig. 5.5a) over the wavelength range 600–800 nm. Figure reproduced with permission: [33] from Copyright 2015 Wiley-VCH

optimal structure showed 2.8 and 3.3 increase in collected power compared to coverslip for in-plane and perpendicular dipole orientations, respectively.

In order to understand the theoretical potential of HMMs for enhancing dipole emission, we estimated the Purcell factor F_P increase as function of the separation distance h between the emitter and the surface. This increase is a common feature for dipoles located near metallic surfaces [41] and is expected to be observed as well in the case of an NV center on HMM. In our case, the smallest separation distance is dictated by the ND size. The Purcell factor dependence on h is explained by the fact that at short distances the evanescent fields created by the emitter are better coupled to the metamaterials modes and non-radiative excitations in the metallic layers [39].

We have calculated the Purcell factor as a function of h for different orientations of a dipole located in the homogeneous medium above the HMM structure previously described (see Fig. 5.10). At the distance of 25 nm, corresponding to the size of our NDs, the Purcell enhancement is on the order of 10, as shown in Fig. 5.5a. However, at distances h of a few nanometers the Purcell factor reaches two orders of magnitude, which corresponds to a spontaneous emission lifetime of 0.1 ns, sufficient for single-photon operation at tens of GHz.

5.4 Lasing Action with Nanorod Hyperbolic Metamaterials

Above, we have discussed the role of HMMs in promoting spontaneous emission from single quantum emitters. Strong spontaneous emission is usually seen as a drawback to observe stimulated emission because it diminishes the inversion

without contributing photons to the lasing mode. Interestingly, due to their rich mode structure, HMMs can be used to promote lasing as well. High Purcell effect for certain metamaterial modes yields a redistribution of spontaneous emission over wavevector space (*k*-space), with light preferentially coupled to the lasing mode and inhibited in other modes [45].

Several plasmonic lasers have already been demonstrated using various geometries [19], such as metal-insulator-metal waveguides [46], whispering gallery cavities [47], core-shell particles [48, 49], nanohole/particle arrays [50–52], semiconductor-dielectric-metal hybrid cavities [53]. These methods generally used geometries with strong cavity resonances to gain Purcell enhancement and hence lasing as described above. The Purcell enhancement arising from the resonance of metallic structures usually exhibits a relatively narrow bandwidth, thus restraining the frequency of lasing to be achieved. An alternative approach to gain Purcell enhancement is based on non-resonant structures, which can be designed by engineering the dispersion of metamaterials. In this work, we report on the use of nanorod-based HMMs to achieve efficient lasing. It has been shown that metamaterials exhibiting hyperbolic properties can support unique optical waves with very small or large mode indices, allowing for stronger light-matter interaction [16] which could enhance lasing. Our nanorod-based metamaterials are composed of vertically aligned gold nanorods coated with a polyvinyl alcohol (PVA) film. To create a sufficient density of emitters for lasing, rather than using NV centers, we embedded Rhodamine 101 (R101) dye molecules into the PVA film (see the sample schematic in Fig. 5.1b). By adjusting the metal fill ratio, the dispersion of the nanorod metamaterial can be tuned from elliptic to hyperbolic. Our experiments show that HMMs exhibit significant enhancement over elliptic metamaterials (EMM), which is consistent with calculations of Purcell enhancement. The nanorod-based metamaterials are suitable for integration with a broad range of optical gain media to achieve lasing at the desired frequency.

As described earlier, HMMs exhibit a singularity in the photonic LDOS, allowing for spontaneous decay rate enhancement of quantum emitters. On the other hand, it has been shown that the Purcell effect could contribute to efficient optical amplification and lasing action, provided that a portion of the enhanced spontaneous emission feeds into the lasing mode [45]. To our knowledge, so far there is only one report that addressed the possibility to achieve stimulated emission from a HMM comprised of Ag and MgF_2 layer stacks [54]. Although a reduced threshold was observed in a HMM when compared to a reference device based on a bare Ag film, the emission efficiency from the HMM was obviously lower than from the reference. Thus, the full potential of HMM to achieve lasing with low threshold and high efficiency remained to be explored.

In this work, two gold nanorod arrays embedded in anodic alumina templates have been fabricated, exhibiting hyperbolic (labeled HMM) and elliptic dispersion (labeled EMM) at the emission wavelength of R101 ($\lambda = 606$ nm), according to local EMT. The different dispersion characteristics were achieved by altering the metal fill ratio using different nanorod diameters. Arrays of gold nanorods were fabricated by electrodeposition within nanoporous aluminum oxide membranes.

The membranes were prepared by the anodization in H_2SO_4 of Al films deposited on Au-coated glass substrates. Substrate anodization was performed at 30 V for the HMM and at 25 V for the EMM, to yield approximate pore diameters of 40 and 25 nm respectively, surface densities of 35 % and 14 % respectively, and nanopore heights of 250 nm. Gold nanorods were electrodeposited as previously described under galvanostatic conditions [55] using a current density of 0.5 mA/cm^2, with constant electrodeposition up to the maximum height allowed by the nanoporous alumina templates, at which point a distinct drop in voltage (>20 %) was observed. SEM images of the nanorod-based HMM and EMM substrates indicate that the nanorods have uniform diameters and are well dispersed within the Al_2O_3 matrix, which has an approximate pore-to-pore distance of 60 nm for each sample (see insets of Fig. 5.11a,b).

As follows from 1 and 2 in Table 5.1, the EMT model for nanorod HMMs supports two resonances, specifically the epsilon-near-pole (ENP,$\varepsilon_{\|} \to \infty$) and

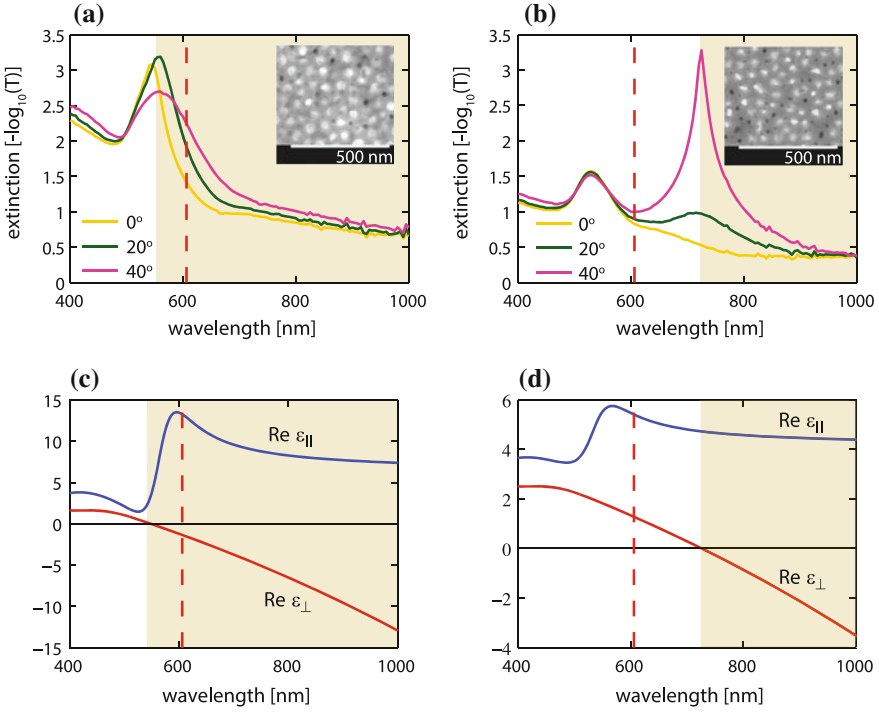

Fig. 5.11 Experimental extinction spectra for **a** HMM and **b** EMM samples. The spectra were obtained using TM–polarized light at 0° (*yellow*), 20° (*green*) and 40° (*pink*) incidence. Effective anisotropic permittivities of **c** HMM and **d** EMM estimated using Maxwell-Garnett theory. *Shaded* regions indicate wavelength range where the metamaterial exhibits hyperbolic Type-I dispersion. *Dotted red line* indicates central emission wavelength of R101 dye (606 nm). SEM scans of the nanorod metamaterials are shown in the *insets*. Figures reproduced with permission: [13] from Copyright 2016 ACS

epsilon-near-zero (ENZ, $\varepsilon_{\perp} \to 0$) responses [56]. The ENP resonance is purely dependent on the permittivities of the metal and dielectric, and hence does not vary with the metal fill ratio. However, the ENZ response (and corresponding dispersion crossover wavelength) can be tuned easily by adjusting the fill ratio. In the case of HMM, only one resonance band is observed since the ENP and ENZ responses overlap starting at $\lambda = 530$ nm, whereas EMM has distinct ENP ($\lambda = 530$ nm) and ENZ ($\lambda = 710$ nm) responses, as seen in Fig. 5.11a, b. Effective Maxwell-Garnett permittivities were calculated based on the fill ratios for each sample (see Fig. 5.11c, d) and the permittivity values of bulk Au and amorphous Al_2O_3. Both the extinction and permittivity plots confirm that the HMM exhibits hyperbolic dispersion and the EMM exhibits elliptic dispersion at the same wavelength as the central emission of R101.

5.4.1 *Purcell Effect Calculations for Dye Molecules on Nanorod Metamaterials*

We estimated the Purcell factors for our HMM and EMM structures by simulating the coupling of dipole emitters with our metamaterials, defined by local EMT. Using the standard Green's function formalism as shown in the previous section, we calculated the Purcell factors for a dipole embedded in PVA (refractive index $n = 1.5$) placed 20 nm above HMM and EMM deposited on glass substrates ($n = 1.5$), as shown in Fig. 5.12a, b. In the calculation, we distinguish between in-plane, perpendicular, and "average" dipole orientations. The calculation results show that the HMM provides a Purcell factor of 5.75 for a dipole parallel to the HMM surface, and 12.21 for a dipole perpendicular to the surface at the central wavelength of R101 ($\lambda = 606$ nm). On the other hand, the EMM provides a Purcell factor of 1.5 and 2.15 for parallel and perpendicular orientations, respectively. On average the HMM provides an enhancement of 4.6 times over the EMM. The calculation also shows that the Purcell factor strongly depends on the distance of the dipole from the metamaterial surface (see Fig. 5.12c), as it was already discussed for the planar HMM case. For dipoles very close to the metamaterial surface (~5 nm), the Purcell factor for the HMM is extremely large, reaching up to 400, while the EMM only provides an enhancement of 46. As the dipole is moved away from the surface, the Purcell factor for the EMM decays much quicker than that for HMM, reaching ~1 within a 40 nm distance, while it is still slightly larger than 1 for the HMM at a distance of 100 nm.

In order to further study the decay channels providing this Purcell enhancement, we have also calculated the inherent plasmonic modes (named as high-k modes) that can be excited in our HMM and EMM structures. Figure 5.13 shows the *k*-space dissipated power density, $\log_{10}\left[k_0 dF_P^{ave}/dk_{||}\right]$, calculated for a dipole with the averaged orientation, located 20 nm above the surface of HMM and EMM, defined by local EMT. In both HMM and EMM, we can see the modal gap, i.e., wavelength

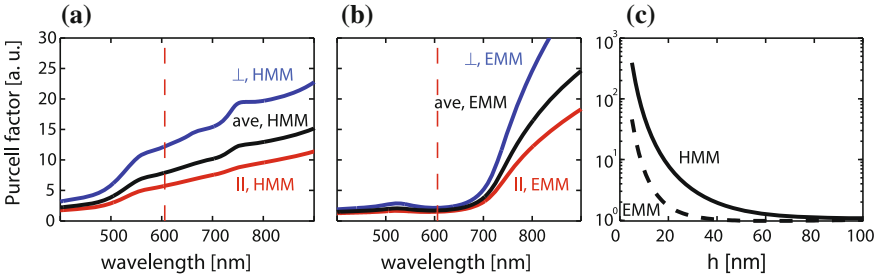

Fig. 5.12 Theoretical estimations of Purcell factor versus emission wavelength for a dipole located 20 nm above HMM (**a**) and EMM (**b**), as well as the Purcell factor dependences on the distance of dipole from metamaterial surface (**c**) at emission wavelength of 606 nm (indicated with a *red dashed line* in (**a**) and (**b**)). *Blue*, *red*, and *black curves* in (**a**) and (**b**) refer to dipoles oriented perpendicular, parallel to the metamaterial surface, and averaged, respectively. The Purcell factor in (**c**) is plotted for the averaged dipole orientation. Figures reproduced with permission: [13] from Copyright 2016 ACS

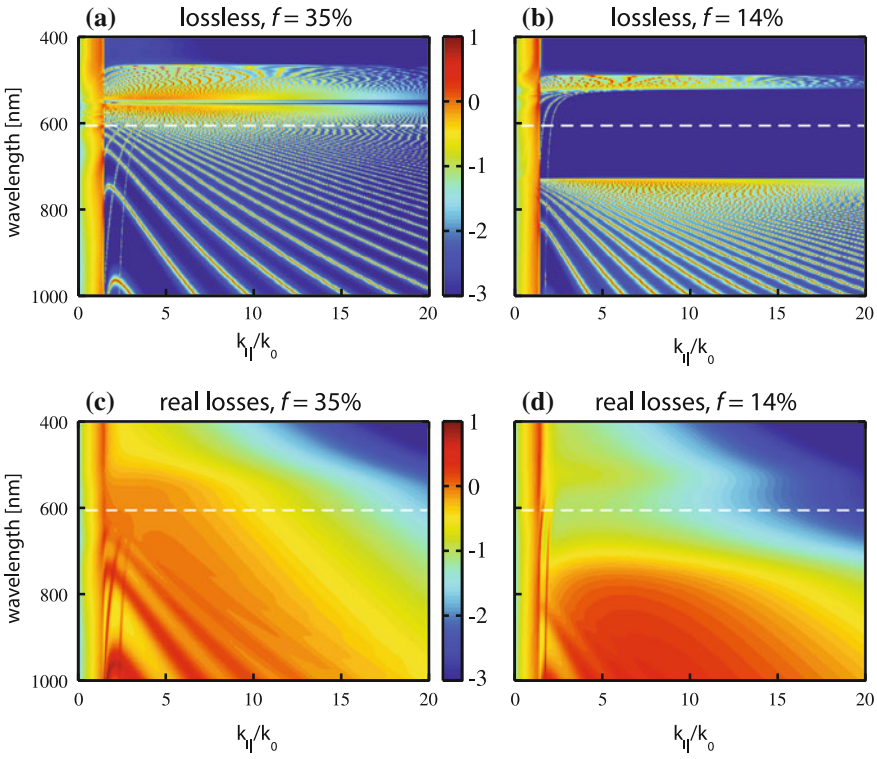

Fig. 5.13 *k*-space dissipated power density for a dipole placed 20 nm above HMM (**a**) and EMM (**b**), without losses. Subfigures (**c**) and (**d**) correspond to the cases of (**a**) and (**b**) with actual losses. At 606 nm (*white dotted line*), HMM provides many more inherent plasmonic modes than EMM. Figures reproduced with permission: [13] from Copyright 2016 ACS

range where very few plasmonic modes are allowed between ENP and ENZ resonances. We see that at 606 nm, EMM falls in this modal gap with almost no propagating modes, while HMM provides much more modes to enhance the emitter's decay rate, for even very large $k_{||}$ (in-plane wavevector). Due to this large number of allowed modes, we clearly see that our HMM provides significant Purcell enhancement over our EMM structure, and is therefore expected to enhance spontaneous emission greatly, which could feed into lasing modes.

5.4.2 *Experimental Demonstration of Lasing with Nanorod Metamaterials*

The nanorod arrays were spin coated with a 10 mM solution of R101 dye dissolved in PVA at 1000 rpm for 30 s followed by baking at 60 °C for 6 h, which yielded a ~2 μm thick film. A frequency-doubled Nd:YAG picosecond laser (532 nm emission wavelength, 400 ps pulse width and 1 Hz repetition rate) was used to pump the samples at 40°. The pump pulses were focused down to a spot size of ~200 μm in diameter using a 5× objective lens. The emission from the samples was collected with a fiber almost normal to the sample surface, which was fed to a spectrometer equipped with a charge-coupled device.

Figure 5.14a, b show the evolution of the emission spectra with the pump energy for both HMM and EMM. Obvious spectral narrowing was observed for both HMM and EMM when the pump energy was increased up to ~3.2 μJ and 4.0 μJ respectively. At a pump energy of ~5.5 μJ, the emission intensity from HMM was twice as strong as that from EMM. From the plot of pump-dependent peak emission intensity (see Fig. 5.14c, d), we can see a clear threshold for the two systems, with HMM having a lower threshold (~3.2 μJ) than EMM (4 μJ). We attribute the increase in collected emission intensity mainly to the Purcell enhancement, which couples spontaneous emission into lasing modes. Furthermore, it has been reported that the interactions between nanorods may form cavities to provide feedback [52], which could play a role in the occurrence of lasing. In addition, the nonlocal optical waves exhibited in the nanorod medium could enhance spontaneous emission, which could affect lasing action in such metamaterials [16].

As control samples, we studied the emission from a bare glass substrate and a 250-nm thick gold film, both coated with R101 in PVA. Both samples only showed spontaneous emission, without any evident spectral narrowing (see Fig. 5.15a, b). As a comparison, we fabricated a lamellar HMM with ten alternating layers of Au (8.9 nm) and Al_2O_3 (16.1 nm), which has the same metal fill ratio (35 %) and thickness (250 nm) as the nanorod-based HMM. We applied the gain medium and conducted lasing measurements in the same way as described above and enhanced emission was collected from the sample based on the multilayer-based HMM; however, no lasing was observed, as shown in Fig. 5.15c.

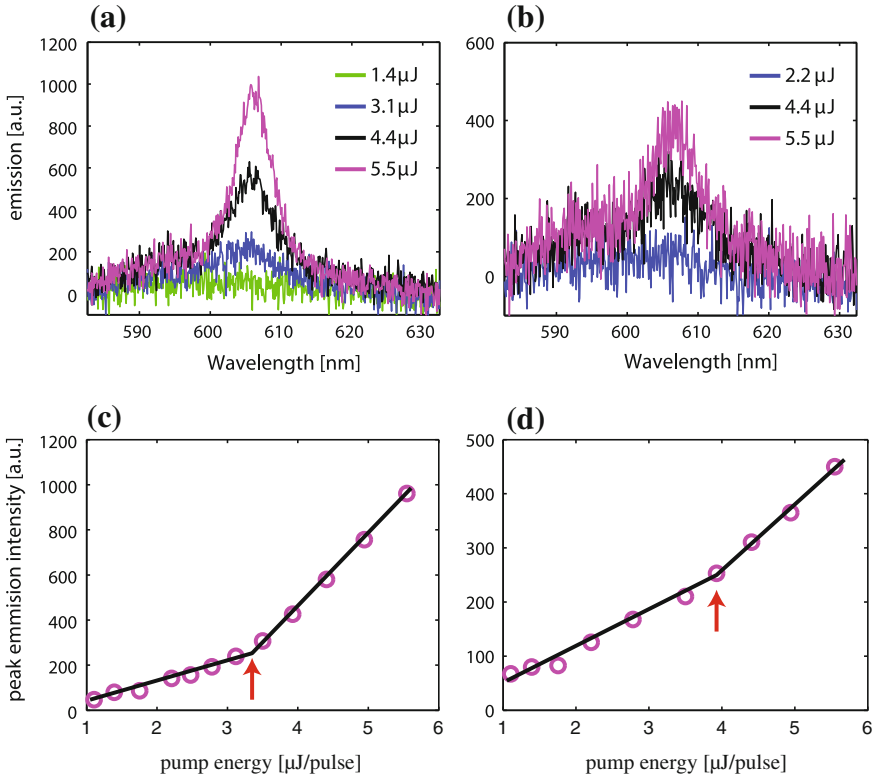

Fig. 5.14 Emission spectra for **a** HMM and **b** EMM at various laser pumping energies. Peak intensity plots for **c** HMM and **d** EMM; the slope kinks correspond to the lasing threshold energy (*red arrows*). *Lines* in **c** and **d** are least-squares fits. Figures reproduced with permission: [13] from Copyright 2016 ACS

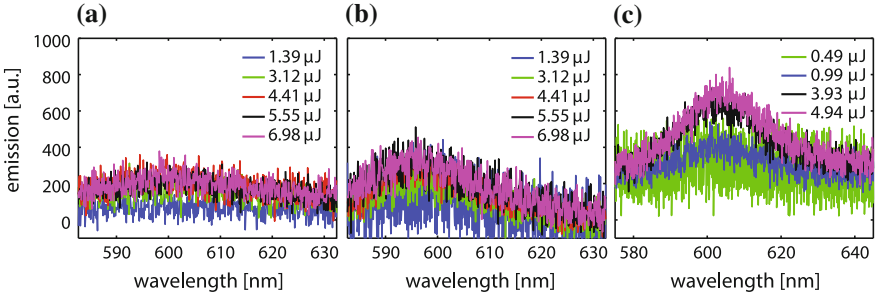

Fig. 5.15 Emission from control **a** glass and **b** gold film samples, as well as **c** lamellar HMM composed of 10 pairs of 8.9 nm gold film and 16.1 nm alumina film, all coated with R101 in PVA. Plots show amplified spontaneous emission, but no threshold behavior for lasing. Figures reproduced with permission: [13] from Copyright 2016 ACS

Therefore, the nanorod-based HMM provides a significant enhancement over its lamellar counterpart, exhibiting low-threshold lasing action. Furthermore, infusion of dyes directly into the matrix of the nanorod-based HMM is far more feasible than embedding them within the lamellar HMM. This should greatly enhance the emitter-field coupling and spontaneous emission, and lead to much lower thresholds for lasing, which is currently under investigation.

5.5 Summary

The chapter explores the opportunities offered by hyperbolic metamaterials to promote both spontaneous and stimulated emission. We have demonstrated implementations of an efficient single-photon source and a plasmonic laser using two different metamaterials designs. We have experimentally demonstrated an improvement in the emission properties of single NV center nanodiamonds placed on top of an epitaxial TiN/(Al,Sc)N HMM compared to a glass substrate. The observed lifetime decreased by a factor of 4, which is in good agreement with theoretical prediction. The collected emission power for NV centers near the HMM increased by a factor of 1.8 on average, although an extremely high enhancement of 4.7 was detected in one particular case. The emission rate could be further enhanced by the presence of an adjacent HMM defect or a deterministically engineered outcoupling feature such as a circular groove.

In a similar fashion, we have demonstrated lasing action supported by metamaterials based on gold nanorod arrays coated with thin films of PVA embedded with R101 dye. The metamaterial could be tuned to exhibit hyperbolic (HMM) or elliptic (EMM) dispersion depending on metal fill ratio. Both regimes supported lasing action, with emission from the HMM being twice as strong as that from the EMM while also exhibiting lower threshold. Embedding lasing dyes directly into the nanorod matrix will likely further enhance the emitter-field coupling, and also lower the HMM lasing threshold. The HMM provides broadband Purcell enhancement, suggesting its application as a source for coherent photon emission in a broadband wavelength range.

Acknowledgements This work was partially supported by AFOSR-MURI grant (FA9550-10-1-0264), NSF-MRSEC grant (DMR-1120923), and ONR grant (N00014-13-1-0649).

Appendix: Semi-analytical Calculations of the Purcell Factor and Normalized Collected Emission Power

High LDOS provided by the HMM can lead to dramatic changes in fluorescence lifetimes of quantum emitters. In practice, one is also interested in the percentage of the dissipated optical power that can be collected by a far field detector. In order to

describe effects of a realistic HMM on a single-dipole emitter placed in the vicinity of a planar HMM, we performed calculations of total power flow in the immediate vicinity of the emitter as well as through a far-field collection plane. A single emitter was modeled as an oscillating electric dipole with dipole moment **p** and angular frequency ω. The energy dissipation rate in an inhomogeneous environment is given by [41]

$$P = \frac{\omega}{2}\mathrm{Im}\left[\mathbf{p}^{*}\cdot\left(\mathbf{E}_0(\mathbf{r}_0)+\mathbf{E}_s(\mathbf{r}_0)\right)\right] \tag{A.1}$$

where $\mathbf{E}_0(\mathbf{r}_0)$ and $\mathbf{E}_s(\mathbf{r}_0)$ are the primary dipole field and scattered field at the dipole position (r_0), respectively. These electric fields were calculated using the dyadic Green's function formalism [41]. We analyzed the contribution of each spatial frequency mode using an angular spectrum representation of the Green's functions. The Purcell factors F_P for in-plane (∥) and perpendicular (⊥) oriented single-dipole emitters placed at a distance h above a multilayer planar structure were calculated using the following formulae [41]

$$F_P^{\perp} = 1 + \frac{3}{2}\frac{1}{\varepsilon_{\mathrm{sup}}^{3/2}}\int_0^{\infty}\mathrm{Re}\left\{\frac{s^3}{s_{\perp,\,\mathrm{sup}}(s)}\tilde{r}^{\mathrm{p}}(s)e^{2ik_0 s_{\perp,\,\mathrm{sup}}(s)h}\right\}ds \tag{A.2}$$

$$F_P^{\parallel} = 1 + \frac{3}{4}\frac{1}{\varepsilon_{\mathrm{sup}}^{1/2}}\int_0^{\infty}\mathrm{Re}\left\{\frac{s}{s_{\perp,\,\mathrm{sup}}(s)}\left[\tilde{r}^{\mathrm{s}}(s)-\frac{s_{\perp,\,\mathrm{sup}}^2(s)}{\varepsilon_{\mathrm{sup}}}\tilde{r}^{p}(s)\right]e^{2ik_0 s_{\perp,\,\mathrm{sup}}(s)h}\right\}ds \tag{A.3}$$

The value of F_P for the isotropic (ave), statistically averaged dipole orientation is given by

$$F_P^{ave} = \frac{2}{3}F_P^{\parallel} + \frac{1}{3}F_P^{\perp} \tag{A.4}$$

Normalized collected emission powers f_{rad} for the same dipole orientations are shown below

$$f_{rad}^{\perp} = \frac{3}{4}\int_0^{\theta_{\max}}\sin^3\theta\left|e^{-i\varepsilon_{\mathrm{sup}}^{1/2}k_0 h\cos\theta}+\tilde{r}^{\mathrm{p}}(\theta)e^{i\varepsilon_{\mathrm{sup}}^{1/2}k_0 h\cos\theta}\right|^2 d\theta \tag{A.5}$$

$$f_{rad}^{\parallel} = \frac{3}{8}\int_0^{\theta_{\max}}\cos^2\theta\left|e^{-i\varepsilon_{\mathrm{sup}}^{1/2}k_0 h\cos\theta}-\tilde{r}^{\mathrm{p}}(\theta)e^{i\varepsilon_{\mathrm{sup}}^{1/2}k_0 h\cos\theta}\right|^2+\left|e^{-i\varepsilon_{\mathrm{sup}}^{1/2}k_0 h\cos\theta}+\tilde{r}^{\mathrm{s}}(\theta)e^{i\varepsilon_{\mathrm{sup}}^{1/2}k_0 h\cos\theta}\right|^2\sin\theta d\theta \tag{A.6}$$

$$f_{rad}^{ave} = \frac{2}{3}f_{rad}^{\parallel} + \frac{1}{3}f_{rad}^{\perp} \tag{A.7}$$

In equations A.2–A.7, $s = k_{\|}/k_0$, $s_{\perp,\,\mathrm{sup}}(s) = k_{\perp,\,\mathrm{sup}}(s)/k_0 = \left(\varepsilon_{\mathrm{sup}} - s^2\right)^{1/2}$, $k_0 = \omega/c$, θ is a polar angle measured from the $\perp$ direction, the collection angle $\theta_{\max} = 79.6°$. $k_{\|}$ is the in-plane component of the k-vector varying from 0 to infinity. $\tilde{r}^p$ and $\tilde{r}^s$ are generalized superlattice's Fresnel reflection coefficients for p- and s-polarized light. The reflection coefficients were calculated utilizing the recursive imbedding method [42, 57]. The integrals were numerically evaluated by using an adaptive Gauss-Kronrod quadrature method [58]. In the formulae, we assumed that intrinsic quantum yield of NV centers is close to unity [59]. F_P and f_{rad} were normalized by the total radiation power and the power emitted into the collection angle, respectively. Both powers corresponded to the case of the emitter immersed into homogeneous medium with dielectric permittivity $\varepsilon_{\mathrm{sup}}$, which models well the reference sample in the experiment.

References

1. P.C. Clemmow, The theory of electromagnetic waves in a simple anisotropic medium. Proc. Inst. Electr. Eng. **110**(1), 101 (1963)
2. R.H. Ritchie, Plasma losses by fast electrons in thin films. Phys. Rev. **106**(5), 874–881 (1957)
3. S.M. Rytov, Electromagnetic properties of a finely stratified medium. Sov. Phys. JETP **2**(10) (1956)
4. D. Smith, D. Schurig, Electromagnetic wave propagation in media with indefinite permittivity and permeability tensors. Phys. Rev. Lett. **90**(7), 077405 (2003)
5. Z. Jacob, L.V. Alekseyev, E. Narimanov, Optical hyperlens: far-field imaging beyond the diffraction limit. Opt. Express **14**(18), 8247–8256 (2006)
6. Z. Liu, H. Lee, Y. Xiong, C. Sun, X. Zhang, Far-field optical hyperlens magnifying sub-diffraction-limited objects. Science **315**(5819), 1686 (2007)
7. S. Ishii, A.V. Kildishev, E. Narimanov, V.M. Shalaev, V.P. Drachev, Sub-wavelength interference pattern from volume plasmon polaritons in a hyperbolic medium. Laser Photon. Rev. **7**(2), 265–271 (2013)
8. Z. Jacob, J.-Y. Kim, G.V. Naik, A. Boltasseva, E.E. Narimanov, V.M. Shalaev, Engineering photonic density of states using metamaterials. Appl. Phys. B **100**(1), 215–218 (2010)
9. A.D. Neira, N. Olivier, M.E. Nasir, W. Dickson, G.A. Wurtz, A.V Zayats, Eliminating material constraints for nonlinearity with plasmonic metamaterials. Nat. Commun. **6**, 7757 (2015)
10. S.-A. Biehs, M. Tschikin, P. Ben-Abdallah, Hyperbolic metamaterials as an analog of a blackbody in the near field. Phys. Rev. Lett. **109**(10), 104301 (2012)
11. C. Shen, Y. Xie, N. Sui, W. Wang, S.A. Cummer, Y. Jing, Broadband acoustic hyperbolic metamaterial. Phys. Rev. Lett. **115**(25), 1–5 (2015)
12. E.E. Narimanov, A.V. Kildishev, Naturally hyperbolic. Nat. Photonics **9**, 214–216 (2015)
13. R. Chandrasekar, Z. Wang, X. Meng, M.Y. Shalaginov, A. Lagutchev, Y.L. Kim, A. Wei, A. V. Kildishev, A. Boltasseva, V.M. Shalaev, Lasing action with gold nanorod hyperbolic metamaterials. arXiv:1609.05168 (2016)
14. G.V Naik, B. Saha, J. Liu, S.M. Saber, E.A. Stach, J.M.K. Irudayaraj, T.D. Sands, V.M. Shalaev, A. Boltasseva, Epitaxial superlattices with titanium nitride as a plasmonic component for optical hyperbolic metamaterials. Proc. Natl. Acad. Sci. **111**(21), 7546–7551 (2014)
15. J. Elser, R. Wangberg, V.A. Podolskiy, E.E. Narimanov, Nanowire metamaterials with extreme optical anisotropy. Appl. Phys. Lett. **89**(26), 261102 (2006)

16. B.M. Wells, A.V. Zayats, V.A. Podolskiy, Nonlocal optics of plasmonic nanowire metamaterials. Phys. Rev. B **89**(3), 35111 (2014)
17. A.V. Chebykin, A.A. Orlov, A.V. Vozianova, S.I. Maslovski, Y.S. Kivshar, P.A. Belov, Nonlocal effective medium model for multilayered metal-dielectric metamaterials. Phys. Rev. B **84**(11), 115438 (2011)
18. M.D. Eisaman, J. Fan, A. Migdall, S.V. Polyakov, Invited review article: single-photon sources and detectors. Rev. Sci. Instrum. **82**(7), 071101 (2011)
19. R.-M. Ma, R.F. Oulton, V.J. Sorger, X. Zhang, Plasmon lasers: coherent light source at molecular scales. Laser Photonics Rev. **7**(1), 1–21 (2013)
20. C. Monroe, Quantum information processing with atoms and photons. Nature **416**(6877), 238–246 (2002)
21. D. DiVincenzo, Quantum computation. Science **270**(5234), 255–261 (1995)
22. N. Gisin, G. Ribordy, H. Zbinden, Quantum cryptography. arXiv Prepr. quant-ph/0101098 (2001)
23. L.M. Duan, M.D. Lukin, J.I. Cirac, P. Zoller, Long-distance quantum communication with atomic ensembles and linear optics. Nature **414**(6862), 413–418 (2001)
24. D. Bouwmeester, J. Pan, K. Mattle, M. Eibl, H. Weinfurter, A. Zeilinger, Experimental quantum teleportation. 575–579 (1997)
25. A. Gruber, A. Dräbenstedt, C. Tietz, L. Fleury, J. Wrachtrup, C. von Borczyskowski, Scanning confocal optical microscopy and magnetic resonance on single defect centers. Science **276**(5321), 2012–2014 (1997)
26. C. Kurtsiefer, S. Mayer, P. Zarda, H. Weinfurter, Stable solid-state source of single photons. Phys. Rev. Lett. **85**(2), 290–293 (2000)
27. P. Tamarat, T. Gaebel, J.R. Rabeau, M. Khan, A.D. Greentree, H. Wilson, L.C.L. Hollenberg, S. Prawer, P. Hemmer, F. Jelezko, J. Wrachtrup, Stark shift control of single optical centers in diamond **083002**, 1–4 (2006)
28. G. Fuchs, V. Dobrovitski, R. Hanson, A. Batra, C. Weis, T. Schenkel, D. Awschalom, Excited-state spectroscopy using single spin manipulation in diamond. Phys. Rev. Lett. **101** (11), 117601 (2008)
29. E.M. Purcell, Spontaneous emission probabilities at radio frequencies. Phys. Rev. **69** (1946)
30. S. Schietinger, O. Benson, Coupling single NV-centres to high-Q whispering gallery modes of a preselected frequency-matched microresonator. J. Phys. B: At. Mol. Opt. Phys. **42**(11), 114001 (2009)
31. J. Riedrich-Möller, L. Kipfstuhl, C. Hepp, E. Neu, C. Pauly, F. Mücklich, A. Baur, M. Wandt, S. Wolff, M. Fischer, S. Gsell, M. Schreck, C. Becher, One- and two-dimensional photonic crystal microcavities in single crystal diamond. Nat. Nanotechnol. **7**(1), 69–74 (2012)
32. A. Faraon, C. Santori, Z. Huang, V.M. Acosta, R.G. Beausoleil, Coupling of nitrogen-vacancy centers to photonic crystal cavities in monocrystalline diamond. Phys. Rev. Lett. **109**(3), 033604 (2012)
33. M.Y. Shalaginov, V.V. Vorobyov, J. Liu, M. Ferrera, A.V. Akimov, A. Lagutchev, A.N. Smolyaninov, V.V. Klimov, J. Irudayaraj, A.V. Kildishev, A. Boltasseva, V.M. Shalaev, Enhancement of single-photon emission from nitrogen-vacancy centers with TiN/(Al,Sc)N hyperbolic metamaterial. Laser Photon. Rev. **9**(1), 120–127 (2015)
34. M.Y. Shalaginov, S. Ishii, J. Liu, J. Liu, J. Irudayaraj, A. Lagutchev, A.V. Kildishev, V.M. Shalaev, Broadband enhancement of spontaneous emission from nitrogen-vacancy centers in nanodiamonds by hyperbolic metamaterials. Appl. Phys. Lett. **102**(17), 173114 (2013)
35. D. Lu, J.J. Kan, E.E. Fullerton, Z. Liu, Enhancing spontaneous emission rates of molecules using nanopatterned multilayer hyperbolic metamaterials. Nat. Nanotechnol. **9**(1), 48–53 (2014)
36. H.N.S. Krishnamoorthy, Z. Jacob, E. Narimanov, I. Kretzschmar, V.M. Menon, Topological transitions in metamaterials. Science **336**(6078), 205–209 (2012)

37. T. Galfsky, H.N.S. Krishnamoorthy, W. Newman, E.E. Narimanov, Z. Jacob, V.M. Menon, Active hyperbolic metamaterials: enhanced spontaneous emission and light extraction. Optica **2**(1), 62 (2015)
38. G.V. Naik, J.L. Schroeder, X. Ni, V. Alexander, T.D. Sands, A. Boltasseva, Titanium nitride as a plasmonic material for visible and near-infrared wavelengths. Opt. Mater. Express **2**(4), 534–537 (2012)
39. Z. Jacob, I.I. Smolyaninov, E.E. Narimanov, Broadband Purcell effect: radiative decay engineering with metamaterials. Appl. Phys. Lett. **100**(18), 181105 (2012)
40. M.S. Yeung, T.K. Gustafson, Spontaneous emission near an absorbing dielectric surface. Phys. Rev. A **54**(6), 5227–5242 (1996)
41. L. Novotny, B. Hecht, *Principles of nano-optics* (Cambridge University Press, Cambridge, 2006)
42. W.C. Chew, S. Chen, Response of a point source embedded in a layered medium. IEEE Antennas Wirel. Propag. Lett. **2**(1), 254–258 (2003)
43. K. Visscher, G.J. Brakenhoff, T.D. Visser, J. Microsc. **175**(2), 162–165 (1994)
44. S.V. Zhukovsky, O. Kidwai, J.E. Sipe, Opt. Express **21**(12), 14982–14987 (2013)
45. M.P. van Exter, G. Nienhuis, J.P. Woerdman, Two simple expressions for the spontaneous emission factor β. Phys. Rev. A **54**(4), 3553–3558 (1996)
46. M.T. Hill, M. Marell, E.S.P. Leong, B. Smalbrugge, Y. Zhu, M. Sun, P.J. van Veldhoven, E. J. Geluk, F. Karouta, Y.-S. Oei, R. Nötzel, C.-Z. Ning, M.K. Smit, Lasing in metal-insulator-metal sub-wavelength plasmonic waveguides. Opt. Express **17**(13), 11107 (2009)
47. S.-H. Kwon, J.-H. Kang, C. Seassal, S.-K. Kim, P. Regreny, Y.-H. Lee, C.M. Lieber, H.-G. Park, Subwavelength plasmonic lasing from a semiconductor nanodisk with silver nanopan cavity. Nano Lett. **10**(9), 3679–3683 (2010)
48. M.A. Noginov, G. Zhu, A.M. Belgrave, R. Bakker, V.M. Shalaev, E.E. Narimanov, S. Stout, E. Herz, T. Suteewong, U. Wiesner, Demonstration of a spaser-based nanolaser. Nature **460** (7259), 1110–1112 (2009)
49. X. Meng, A.V. Kildishev, K. Fujita, K. Tanaka, V.M. Shalaev, Wavelength-tunable spasing in the visible. Nano Lett. **13**(9), 4106–4112 (2013)
50. W. Zhou, M. Dridi, J.Y. Suh, C.H. Kim, D.T. Co, M.R. Wasielewski, G.C. Schatz, T.W. Odom, Lasing action in strongly coupled plasmonic nanocavity arrays. Nat. Nanotechnol. **8**, 506–511 (2013)
51. F. van Beijnum, P.J. van Veldhoven, E.J. Geluk, M.J.A. de Dood, G.W. 't Hooft, M.P. van Exter, Surface plasmon lasing observed in metal hole arrays. Phys. Rev. Lett. **110**(20), 206802 (2013)
52. X. Meng, J. Liu, A.V. Kildishev, V.M. Shalaev, Highly directional spaser array for the red wavelength region. Laser Photonics Rev. **8**(6), 896–903 (2014)
53. R.F. Oulton, V.J. Sorger, T. Zentgraf, R.-M. Ma, C. Gladden, L. Dai, G. Bartal, X. Zhang, Plasmon lasers at deep subwavelength scale. Nature **461**(7264), 629–632 (2009)
54. J.K. Kitur, L. Gu, T. Tumkur, C. Bonner, M.A. Noginov, Stimulated emission of surface plasmons on top of metamaterials with hyperbolic dispersion. ACS Photonics **2**(8), 1019–1024 (2015)
55. J.-M. Moon, A. Wei, Uniform gold nanorod arrays from polyethylenimine-coated alumina templates. J. Phys. Chem. B **109**(49), 23336–23341 (2005)
56. R. Starko-Bowes, J. Atkinson, W. Newman, H. Hu, T. Kallos, G. Palikaras, R. Fedosejevs, S. Pramanik, Z. Jacob, Optical characterization of epsilon-near-zero, epsilon-near-pole, and hyperbolic response in nanowire metamaterials. J. Opt. Soc. Am. B **32**(10), 2074 (2015)

57. M.Y. Shalaginov, S. Bogdanov, V.V Vorobyov, A.S. Lagutchev, A.V. Kildishev, A.V. Akimov, A. Boltasseva, V.M. Shalaev, Chapter 6: Enhancement of single-photon sources with metamaterials. In: From Atomic to Mesoscale: The Role of Quantum Coherence in Systems of Various Complexities, ed. by S.A. Malinovskaya and I. Novikova, World Scientific, 123–148 (2015)
58. L.F. Shampine, Vectorized adaptive quadrature in MATLAB. J. Comput. Appl. Math. **211**(2), 131–140 (2008)
59. M. Frimmer, A. Mohtashami, A.Femius Koenderink, Nanomechanical method to gauge emission quantum yield applied to nitrogen-vacancy centers in nanodiamond. Appl. Phys. Lett. **102**(12), 121105 (2013)